Amine-grafted H-MFI zeolite precursors as acidic-basic catalysts for deacetalization-Knoevenagel condensation

Iago William Zapelini, Laura Lorena da Silva, Svetlana Mintova, Dilson Cardoso

Amine-grafted H-MFI zeolite precursors as acidic-basic catalysts for deacetalization-Knoevenagel condensation

Iago William Zapelini[a,b], Laura Lorena da Silva[c], Svetlana Mintova[b], Dilson Cardoso[a]

[a] Laboratório de Catálise, Universidade Federal de São Carlos - São Carlos 13565-905, Brasil.

[b] Laboratoire Catalyse et Spectrochimie, ENSICAEN, Université de Caen - Caen 14050, France.

[c] Grupo de Pesquisa em Catálise, Instituto de Química, Universidade Estadual Paulista - Araraquara 14800-900, Brasil.

Abstract

Amorphous and semi-crystalline precursors of zeolites have a large number of silanols that can be used to anchor organic functionalities, like silane-based amines, resulting in formation of basic sites. This work describes the use of amorphous and semi-crystalline precursors of H-MFI zeolite reacting with aminopropyltrimethoxysilane (APTMS) to produce bifunctional acidic-basic catalysts for the deacetalization-Knoevenagel condensation. The effect of precursors crystallinity on the catalytic performance is explained by the formation of Brønsted acidic sites, which catalyze the deacetalization step, and on the propylamine anchoring capacity, controlled by the amount of silanols present in the aluminosilicate. It is shown that the aluminosilicates with lower crystallinity provide a higher yield of the end product ethyl trans-α-cyanocinnamate due to the greater number of grafted propylamine groups. These results provide new insights into the preparation of acidic-basic catalysts for converting bulky molecules.

Introduction

Bifunctional catalysts have received special attention due to their ability to carry out a series reactions in a single reactor by reducing process time, controlling the generation of by-products, and optimizing of purification and separation of chemical intermediates [1]. An important class of these bifunctional catalysts is a material with acid-base properties, capable of activating electrophiles and nucleophiles. This property of the catalysts allows the application in several important reactions, such as the conversion of glucose into hydroxymethylfurfural (HMF), an intermediate for the synthesis of several biofuels and chemicals [1]. Additionally, the simultaneous synthesis of biodiesel and solketal through triglyceride (vegetable oils) reactions brings adding value to glycerol [2].

When carried out in a homogeneous phase, the efficiency of acid-base catalysis is impaired by the base's natural neutralization of the acid. Inserting these sites on a solid support, such as mesoporous silicas or zeolites, allows to obtain sufficient spatial distance between the sites so that both can play their catalytic role. Regarding the acidic property of zeolites in protonic form, the insertion of organic basic groups, such as amino silanes, is an efficient strategy to obtain active and stable acid-base catalysts [3].

Due to its microporous structure of zeolites, their application in catalysis is limited to reactions that involve molecules with a kinetic diameter smaller than their pores. Furthermore, the functionalization of zeolites by post synthesis approaches can considerably block the pores and hinder the reuse of the catalyst [4]. The results of Ge et al. (2014) [5] showed that the presence of mesopores in H-ZSM-5 grafted with APTMS leaded to a complete conversion of benzaldehyde dimethyl acetal to ethyl trans-α-

cyanocinnamate thus proving that the deacetalization followed by Knoevenagel condensation, is strongly diffusion-limited reaction.

Thus development of strategies towards reducing diffusion limitations in solid catalysts are of vital importance [6]. An efficient approach to enhance mass transport in zeolites is through the generation of mesopores either with post-synthesis treatment strategies (top-down strategies) or even during the zeolite synthesis (bottom-up strategies) [7]. These so-called hierarchically structured zeolites have shown improved catalytic activity in several reactions involving bulky molecules due to increased accessibility to catalytic sites caused by the presence of mesopores [8,9].

Another way to improve the diffusivity of large molecules in zeolites is by reducing the particle size, which increases the external area leading to greater catalytic activities. For example, nanosized NaX zeolit applied in Knoevenagel condensation is shown to be more active than micronized zeolite due to the larger external area [10,11]. The nanosized zeolites can be obtained by modifying the hydrothermal synthesis process of specifically prepared aluminosilicates [12].

In order to evaluate the effect of the hydrothermal treatment time on the crystallinity of zeolites, recent works have shown that partially crystalline zeolites with short-range crystalline order exhibit improved catalytic activity in several reactions of bulky molecules [12–14]. Inagaki et al. (2014) [12] studied the crystallization kinetics of NaX zeolite to relate the different stages of zeolite structure formation with the catalytic activity in the Knoevenagel condensation between benzaldehyde and ethyl cyanoacetate. It was shown that the amorphous aluminosilicates formed during the induction period exhibit increased catalytic activity, with a maximum in the imminence of the formation of the zeolitic structure as observed by X-ray diffraction. Our results on 4A zeolite (Na-LTA) showed the same tendency [15] . Haw et al., 2016 [16] used protonic aluminosilicate precursors of zeolite (H-ZSM-5) in the dealkylation of 1,3,5-triisopropylbenzene, a reaction used to assess the

accessibility of acidic sites. The amorphous zeolite precursors demonstrated greater catalytic activity in the reaction, although they had fewer acidic sites than in the crystalline samples. This behavior was attributed to the greater accessibility of catalytic sites in the amorphous aluminosilicates.

Silva et al. [14] evaluated the properties of Na-MFI with different degrees of crystallinity after ion exchange with NH_4^+ and showed that the number of Brønsted acid sites increased with crystallinity. The formation of the zeolitic structure leads to an increased confinement of acidic sites thus reducing their accessibility for large molecules. This behavior affected the turnover frequencies measured during the ketalization of glycerol to solketal, showing that amorphous materials have greater specific activity due to facile mass transport in the semi-crystalline samples. Similar observation was reported by Haw et al. [16] in the case of 1,3,5-triisopropylbenzene dealkylation.

In several papers have already been shown that during the crystallization of MFI zeolite, silanol groups are consumed, while they exist in greater amount in the amorphous precursors [17]. This indicats that the anchoring capacity of silanes in amorphous aluminosilicates precursors can also be greater. We already have shown that the amorphous and semi-crystalline precursors of Na-LTA zeolite have greater capacity for modification with silanes [18].

In this paper we report on the effect of hydrothermal synthesis time and degree of crystallinity of H-MFI zeolite precursors on the formation of Brønsted acidic sites and on the propylamine grafting capacity. The solids with bifunctional properties were tested in a model reaction consisting of two acid and base catalyzed series, the deacetalization of benzaldehyde dimethyl acetal followed by Knoevenagel condensation with ethyl cyanoacetate.

Materials and methods

Synthesis of amorphous, semi-crystalline and crystalline *Na-MFI samples*

Na-MFI and its amorphous and semi-crystalline precursors were prepared free of an organic structural directing agent using the following molar composition of the precursor as described by Kim et al. in the Verified Syntheses of Zeolitic Materials [19]: 100 SiO_2 : 2 Al_2O_3 : 10 Na_2O : 2250 H_2O. ~~[19].~~ Colloidal silica Ludox HS-40 (Sigma-Aldrich) and sodium aluminate (50-56 % w.t. of Al_2O_3, Sigma-Aldrich) were used as Si and Al sources, respectively. The resulting reaction mixtures were submitted to static hydrothermal synthesis at 170 °C for different times from 0 to 4 days in Teflon-lined stainless-steel autoclaves to obtain solids with different crystallinity degrees.

The NH_4^+-form of the samples were prepared by three consecutive ion exchange steps with 1 $mol.L^{-1}$ solutions of ammonium chloride, using 1 g of powder and 50 mL of solution in each exchange. The samples were then washed with water and calcined at 400 °C for 4 h. These samples were labeled H-x (x means the crystallinity of the sample in H-form based on the X-ray diffraction results).

Post-synthesis grafting of samples with aminopropyltrimethoxysilane

The protonic aluminosilicates with different degree of crystallinity were functionalized with basic sites derived from the aminopropyltrimethoxysilane (APTMS) according to the procedure described in our previous paper [18]. For this purpose, 500 mg of powder were added to 20 mL glass vials with 10 mL of toluene (Sigma-Aldrich, 99.8%) and 4 mL of APTMS (Sigma-Aldrich, 97%). The mixture was kept under stirring for 24 h at 80 °C. The solid was recovered by centrifugation at 10000 rpm with 3 consecutive washing steps with

5 mL of ethanol to remove the residual APTMS. Then, samples were dried in an oven at 60 °C and labeled as NH-x, where x indicates their crystallinity.

Characterization

The samples were characterized by X-ray diffraction (XRD), performed on a Rigaku Miniflex 600 diffractometer with Ni filter, using KαCu radiation (λ = 0.1542 nm), goniometer speed of 10° min^{-1} and scanning angle 2θ from 5° to 50°. The percentage of the MFI phase of each solid was calculated using the Rietveld structure refinement method in the TOPAS® 4.2 software.? Or by comparing the intensity or area of the Bragg peaks?

N_2 adsorption and desorption isotherms were recorded at 77 K (either use K or °C in the entire manuscript???_ on a Micromeritics 3Flex Surface Characterization unit (Norcross, GA). The samples were outgassed under vacuum at 350 ºC. The external surface area and microporous volumes were calculated using the t-plot method [20].

Particle sizes and morphologies of the samples were analyzed by scanning electron microscopy (SEM) using a Tescan Mira I LMH under 20 kV. Transmission electron microscopy (TEM) images were obtained using a FEI TECNAI G² F20 HRTEM microscope.

Inductively coupled plasma mass spectrometry (ICP-MS) measurements were recorded using a 7900 ICP-MS from Agilent Technologies.

In situ FTIR spectroscopic measurements of samples were performed on a self-supported pellet (~20 mg of powder and a diameter of 20 mm); the transmission spectra were recorded with a Thermo Scientific Nicolet iS50 FTIR spectrometer equipped with an MCT detector, at a spectral resolution of 4 cm^{-1}. The samples were degassed at 350 °C for 12 h under vacuum (10^{-5} Torr). The Brønsted and Lewis acid sites were characterized based on the different interactions with pyridine followed by FTIR. The adsorption of

pyridine on Brønsted acid sites led to the formation of pyridinium cations ($Py\text{-}H^+$), characterized by an IR band at 1540 cm^{-1}, whereas pyridine adsorbed on Lewis acid sites (Py-L) gave rise to a band at 1450 cm^{-1}. The concentrations of Lewis and Brønsted acid sites were calculated using the Beer−Lambert law, considering extinction coefficients of 1.72 and 1.30 $cm.\mu mol^{-1}$ for the quantification of Py-L and $Py\text{-}H^+$, respectively [21].

Carbon and nitrogen in the functionalized samples were quantified through elemental chemical analysis, carried out in a CHN Analyzer 2400 Serie II Perkin Elmer.

^{29}Si and ^{27}Al magic-angle spinning (MAS) NMR experiments were performed at 99.3 and 130.3 MHz, respectively, on a 500 MHz (11.7 T) Bruker Avance III-HD spectrometer using a 4 mm probe head and spinning rate of 12 kHz. The chemical shifts for Si and Al were referenced to tetramethylsilane (TMS) and $AlCl_3$. Radiofrequency (rf) field strengths of 36 and 50 kHz and recycle delays of 20 and 1 second, respectively were used. Scans of 10240 and 725 for ^{29}Si and ^{27}Al nucleus, respectively were collected.

Catalytic tests

The catalytic activities of APTMS-grafted aluminosilicate samples (NH-x) were assessed by the deacetalization of benzaldehyde dimethyl acetal (A) to form benzaldehyde (B), followed by the Knoevenagel condensation with ethyl cyanoacetate, producing ethyl trans-alpha-cyanocinnamate (C) (Scheme 1).

The reactions were carried out in 5 mL glass batch reactors with controlled temperature (80 °C) for 2 h and 4 h. The volume of the reaction mixture was 3 mL, with a molar composition of 1 benzaldehyde dimethyl acetal: 1 H_2O and 5 wt.% of catalyst based on benzaldehyde dimethyl acetal feed. All tests were repeated twice, and the conversions were presented as a mean value of each experiment.

Scheme 1. The deacetalization of benzaldehyde dimethyl acetal (A) to benzaldehyde (B) followed by the Knoevenagel condensation with ethyl cyanoacetate to form ethyl trans-α-cyanocinnamate (acrylate) (C).

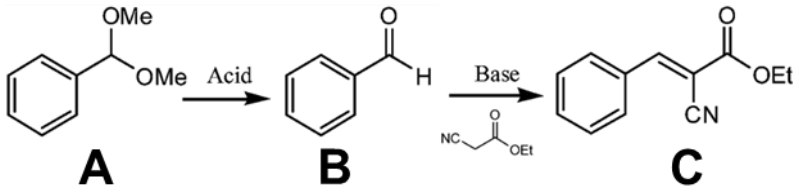

The evolution of reactants and products concentration were monitored by gas chromatography on a Shimadzu GC 2010 equipped with a flame ionization detector (FID), using the separation column RTX-1 (30 m × 0.25 mm x 0.25 μm) of polyethylene glycol stationary phase. Conversions of benzaldehyde dimethyl acetal, reactant **A** (BDA), selectivities and yields of acrylate product **C** were calculated using Equations 1, 2, and 3, respectively, where the number of moles of each compound (n_i) are estimated by calibration curves.

$$X_A = 100\left(\frac{n_{BDA}^0 - n_{BDA}}{n_{BDA}^0}\right) \quad (1)$$

$$S_C = 100\left(\frac{n_C}{n_A^0 - n_A}\right) \quad (2)$$

$$R_C = \frac{X_A . S_C}{100} \quad (3)$$

Results and Discussion

The appearance of the Bragg peaks corresponding to the MFI type zeolite was followed by XRD; the pattern of the H-7 sample is shown in Figure 1*a and* Figure S1*, in Supplementary Material. ?Rietveld refinement confirmed the evolution of the crystallinity of the samples with the hydrothermal treatment (*Table 1

Table *1*), and no other crystalline phases were found in the samples. No amorphous residue was left in the sample H-100, with 100% of crystallinity of ZSM-5 zeolite with an orthorhombic (Pnma) symmetry. XRD measurements also showed that no changes in the crystalline structure of the solids occurred after the functionalization with APTMS; no difference between the XRD patterns recorded for samples H-x and NH-x was observed (Figure S2).

Figure 1. (a) Experimental and Rietveld refined patterns and (b) N_2 physisorption isotherms recorded at 77K for H-x samples (x=0, 7, 12, 56 and 100).

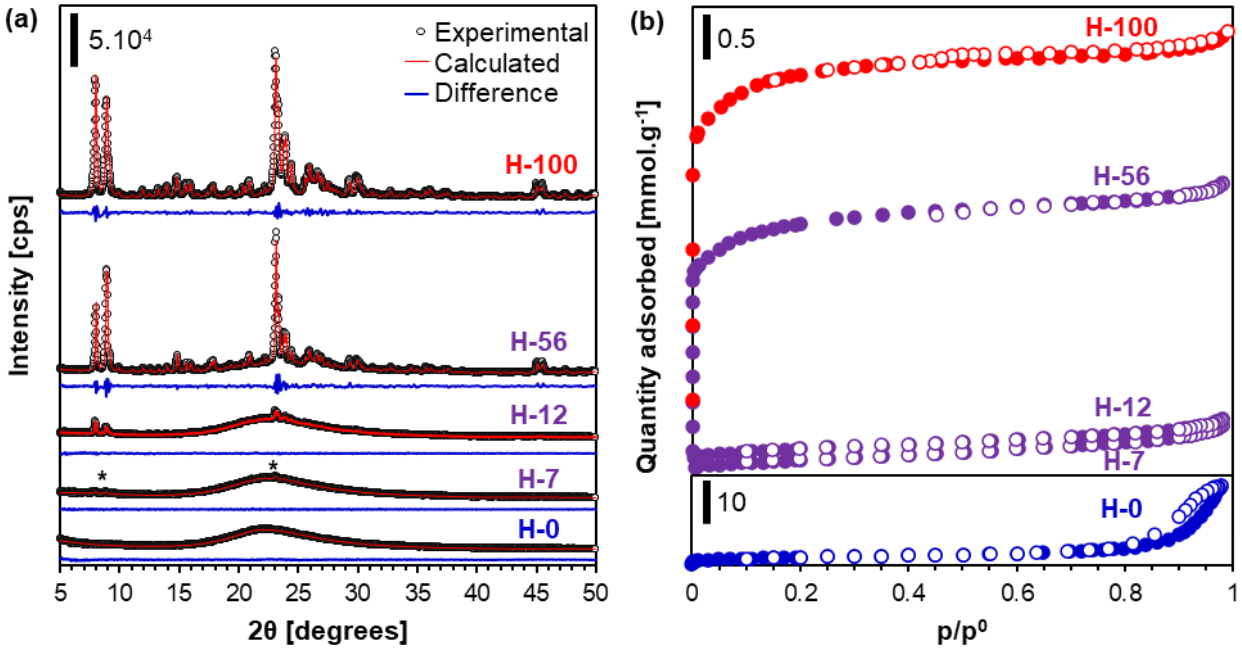

Table 1. Phase quantification and textural properties of samples H-x (x=0, 7, 12, 56 and 100) after different times of hydrothermal synthesis (HT).

Sample	Days of HT	MFI [%] [a]	Amorphous [%] [a]	V_{micro} [$cm^3.g^{-1}$] [b]	S_{ext} [$m^2.g^{-1}$] [b]
H-0	0	0	100	0	133.8

H-7	1	7	93	0.003	9.4
H-12	2	12	88	0.007	8.7
H-56	3	56	44	0.095	6.3
H-100	4	100	0	0.15	5.8

[a] Obtained from Rietveld refinement
[b] Estimated by the N2 adsorption isotherms using the t-plot method.

The formation of the micropores in the solid samples was tracked by nitrogen physisorption (Figure 1b). The starting solid H-0, prepared with no hydrothermal step, presents an isotherm typical for non-porous solids, in which there is no strong interactions between the solid surface and the adsorbate [22]. The high adsorption capacity at $p/p^o \approx 1$ and the hysteresis in the desorption branch in the isotherm of the H-0 sample indicate the presence of interparticle mesoporosity, related to the packing of very small nanoparticles as shown by SEM (Figure 2) and TEM (Figure S4). As the crystallinity of the samples increased, the isotherms were gradually converted to type I, with high adsorption uptake capacity at low partial pressure which is characteristic for microporous solids [22].

Figure 2. SEM images of H-x samples.

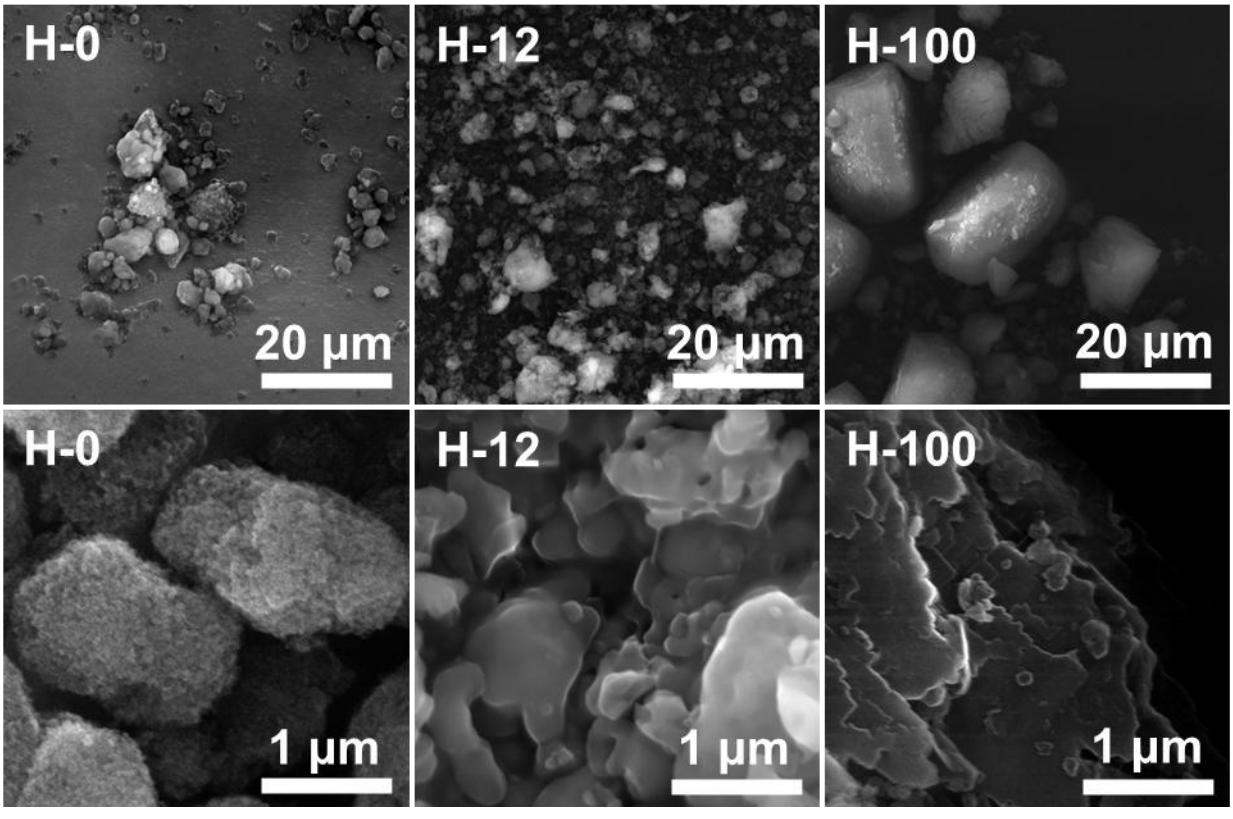

The formation of the microporous structure was followed by the drastic reduction of the interparticle mesoporosity, evidenced by the reduction of the adsorption capacity at $p/p^o \approx 1$ (close to N_2 condensation pressure, Figure 1b). By applying the t-plot method (Figure S3), the increase of microporous volume and the reduction of the external surface area in the samples with different degree of crystallinity was evaluated (Table 1). The disappearance of interparticle mesoporosity, and the abrupt reduction of the external surface area (Table 1), can be explained by the increased particles size of the zeolite crystals. This is supported by SEM results (Figure 2 top) showing that the H-0 sample is formed by the agglomeration of very small nanoparticles (Figure S4), which are converted into non-shaped particles (H-12) with dense glass aspect (Figure S4), and finally prismatic hexagonal particles built by small crystals of MFI zeolite are formed (H-100, Figure 2).

The acidity of the H-x samples were determined by pyridine chemisorption measurements at 150 ºC followed by FTIR. The FTIR spectra of the samples contain two bands (Figure 3a): the band at 1455 cm^{-1} is assigned to pyridine coordinated on Lewis acidic sites (LAS) [23], and the one at 1545 cm^{-1} is due to the vibration of protonated pyridine ($Py\text{-}H^+$) chemisorbed on Brønsted acidic sites (BAS) [24]. The BAS is already present in the amorphous H-0 sample, and the concentration increases as a function of the crystallinity of the samples (Table 2). This can be explained by the incorporation of tetrahedrally coordinated aluminum atoms in the framework of the solids. The increasing amount of Al atoms in the solids as a function of crystallinity if samples is presented in Table 2; the Si/Al ratio of the samples was determined by ICP analyses. The aluminum species in tetrahedral coordination in the zeolite framework are proven by ^{27}Al MAS NMR (Figure 4)

Figure 3. (a) FTIR spectra of H-x samples after thermal desorption of pyridine at 150 °C and 350 °C. (b) Remaining Py-H+ sites on H-x samples after thermal desorption of pyridine at different temperatures.

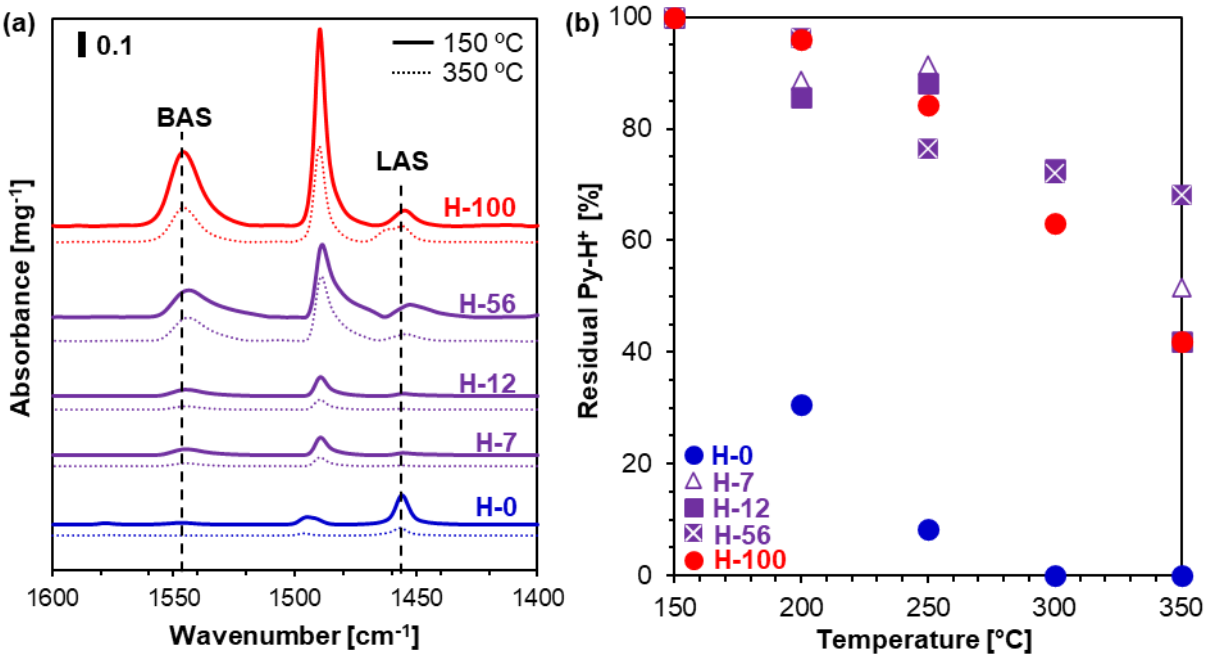

Table 2. Si/Al ratio and acid sites(BAS and LAS) of H-x samples.

Sample	Si/Al [a]	BAS [μmol.g^{-1}] [b]	LAS [μmol.g^{-1}] [b]
H-0	22	7	52.2
H-7	19	8	5.8
H-12	19	31.2	6.5
H-56	19	154.1	42.1
H-100	16	439.3	43.8

[a] Determined by ICP-MS measurements.
[b] Determined by pyridine chemisorption after desorption at 150 ºC based on FTIR.

Due to the high basicity of pyridine, the evaluation of the strength of the acidic sites based on the frequency shift of the stretching modes of pyridine is not possible [14]. Therefore, the pyridine desorption temperature was varied from 150 °C to 350 °C. The number of Brønsted (BAS) and Lewis (LAS) sites remaining after each heating step provides an indirect information for the chemisorption enthalpy of each site. Since the crystallization of the MFI structure started, a big change in the strength of BAS was detected by desorbing pyridine at different temperatures (Figure 3b).

Despite the amorphous precursor H-0, the samples obtained at different crystallization time including the fully-crystalline sample have similar acidic strength of BAS [14]. This similarity between semi-crystalline and fully-crystalline samples can be explained by the short-range crystalline order andsimilar chemical environment of aluminum sites during zeolite growth. As revealed by ^{27}Al MAS NMR spectra (Figure 4), the H-0 sample presents a very broad signal around 55 ppm corresponding to distorted tetrahedrally coordinated aluminum [25]. An increasing intensity and reduction of the broadening of this resonance peak occur along the crystallization time, followed by a shift to lower chemical shifts due to the reduction of T-O-T angles resulting in the formation of a rigid structure [16,26]. The increased local order during the early stages of crystallization leads to the formation of stronger BAS in the semi-crystalline samples.

Figure 4. ^{27}Al MAS NMR spectra of H-x samples.

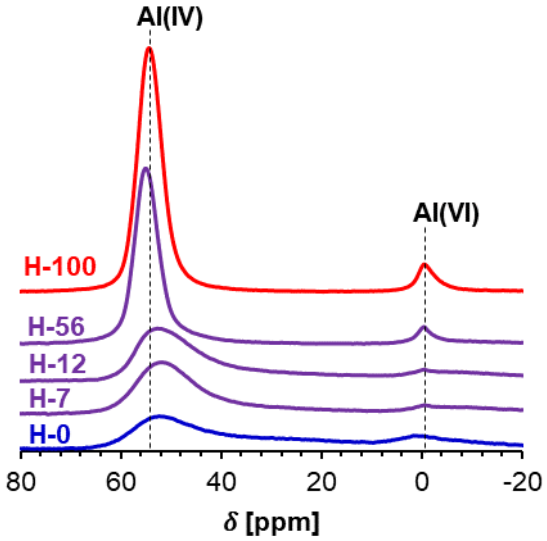

CHN elemental analyses confirmed the presence of nitrogen in the samples after APTMS grafting (Table 3). The amount of nitrogen decreased as a function of samples crystallinity. This implies that propylamine grafting is preferable in the amorphous (NH-0) and semi-crystalline (NH-7,12, 56) than in fully crystalline sample (NH-100). A substantial drop in carbon and nitrogen content is measured from sample NH-0 to NH-7; the nitrogen

content in sample NH-7 is almost half of sample NH-0. This could be attributed to the reduction of silanol defects in the aluminosilicate solids extracted at different crystallization stages. Further the silanol concentration was characterized for all H-x samples. Surprisingly, the number of Q^3+Q^2 species (Q^n = [Si-OT_n-$(OH)_{4-n}$], T = Si or Al), that are due to framework defects [17] slightly increased from H-0 to H-7 and H-12 (Figure 5a), showing that the number of silanols is not disturbing the grafting of samples obtained for short crystallization time (samples ????)

Table 3. Carbon and nitrogen contents of NH-x samples determined by CHN elemental analysis.

Sample	C [mmol.g^{-1}]	N [mmol.g^{-1}]	C/N
NH-0	2.51	0.84	3.0
NH-7	0.91	0.45	2.0
NH-12	1.09	0.26	4.2
NH-56	0.92	0.21	4.4
NH-100	0.74	0.19	3.9

Figure 5. (a) ^{29}Si MAS NMR normalized spectra of H-x samples. (b) FTIR spectra of degassed H-x samples.

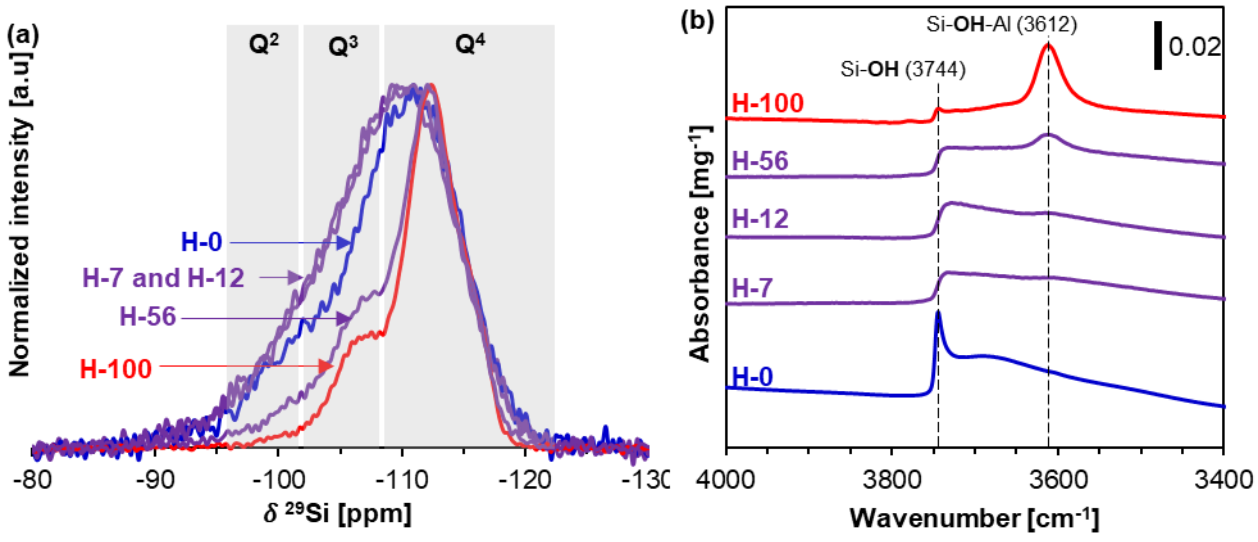

The C/N ratio in the samples was expected to be around 3. The higher C/N values for samples NH-12 to 100 could be explained with the residual non-hydrolyzed methoxy groups from the APTMS or even to the adsorption of atmospheric CO_2 on -NH_2 groups.

Complementary, the silanol sites of degassed samples were characterized by FTIR (Figure 5b). The FTIR results reveal a drastic redistribution of silanol sites in the samples at early stage of zeolite crystallization. Sample H-0 presents a very sharp and intense band related to external silanols at 3744 cm^{-1} [27], which are mostly located on the outer surface of the nanoparticles (Figure S4). In contrast, this signal decreased in the spectrum of sample H-7, and more H-bonded silanols [28] are present, which are similar to samples H-12 to H-100. The bridged hydroxyl groups at 3612 $cm^{-1}$are also detected [29], and the results are in a good agreement with the acidity characterization (see Figure ???). These silanols probably are present inside of the bulky particle [28,30] and therefore they are less accessible for the APTMS molecules. The effect of external silanols on APTMS grafting is revealed [9]. Similar results were reported earlier for Silicalite-1; a strong correlation between external silanols and molybdenum incorporation in the framework was found [30].

^{29}Si MAS NMR spectra were used to confirm the formation of Si-C bonds between aluminosilicates and silane functionalities. The ^{29}Si MAS NMR spectrum of H-0 sample contains a single broad resonance peak associated with non-ordered Q-type sites (Si-O-T bonds) (Figure 6). After the APTMS grafting (NH-0 sample), two additional resonance peaks are visible in the spectrum at -68 ppm and -57 ppm, due to the presence of T^3 sites [H_2N-C_3H_6-Si-$(OSi)_3$], and T^2 sites [H_2N-C_3H_6-Si$(OSi)_2OH$], respectively. This result proves the crosslinking between silane and H-aluminosilicate sample [31]. Further the ^{13}C MAS NMR spectrum of sample NH-0 (Figure S5) provides a direct indication for the presence of propylamine moisture with the appearance of resonance peaks at 10.6, 23.3, and 43 ppm. For fully crystalline NH-100 sample, no changes were observed.

Figure 6. ^{29}Si MAS NMR spectra of amorphous and fully- crystalline samples before (H-0 and H-100) and after APTMS treatment (NH-0 and NH-100.

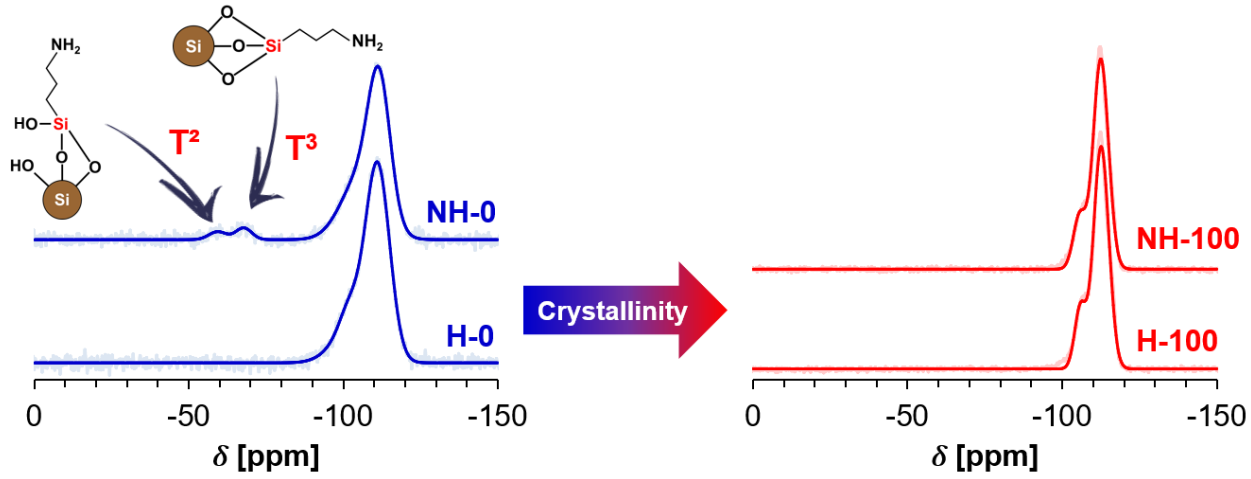

The results from the catalytic test of NH-*x* samples are depicted in Figure 7. Regarding the conversion of benzaldehyde dimethyl acetal (A), which occurs on Brønsted acidic sites, there is an increasing activity of samples as a function of crystallinity; all samples were tested for 2 h (Figure 7a). These results can be explained by the increasing acidity of the samples crystallization with different crystallinity with various amount and strength of BAS (Table 2). By extending the time of the catalytic test, similar BAS strength of semi- (sample ????) and fully crystalline sample (samples ?????) was observed; almost the same conversion after 4 h of reaction was measured, even for the samples with low BAS content.

The turnover frequency (TOF) was used to evaluate the accessibility of BAS in the samples. A pronounced maximum in the TOF when using the NH-7 sample was measured (Figure 7b). The increase in specific activity from NH-0 to NH-7 samples is also attributed to the enhanced strength of BAS as a function of crystallinity degree. On the other hand, despite having the same BAS strength, the NH-12 to NH-100 samples present decreased TOF. This is due to the reduction of the accessibility of BAS confined in the zeolite framework. Similar results were reported earlier [12,14,16,18]. The results suggest that the

crystallization kinetics can be a tool for fine-tuning of TOF of zeolites in acid-catalyzed deacetalization reactions.

Figure 7. Conversions of benzaldehyde dimethyl acetal BDA (a), TOF of BDA (b), selectivity (c) and yields (d) of phenyl acrylate after 2h and 4h of reaction at 80 °C as a function of crystallinity of NH-x samples.

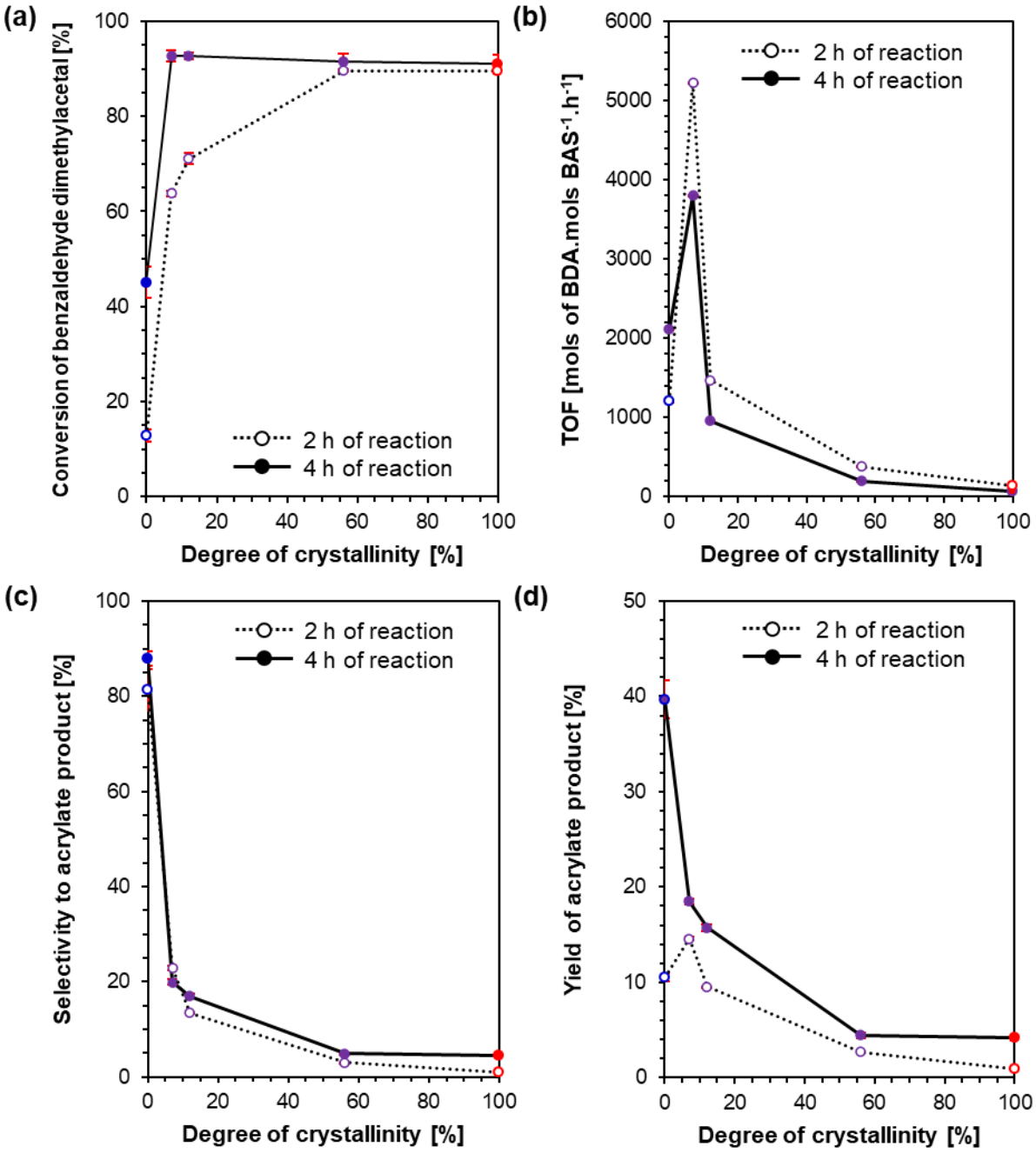

Regarding the activity of propylamine sites, which is described by the selectivity to acrylate product (C), a substantial drop for samples ?????? is observed (Figure 7c), i.e. from ~82% for NH-0 sample to ~24% for NH-7 sample. This behavior is consistent with

nitrogen loading in the samples (Table 3), and the selectivity strongly correlate with the N content (Figure S6). Similar trend for the yield of the end product is observed (Figure 7d), except for the NH-7 sample tested for 2 h, which led to a maximum yield of acrylate. This is due to the strong Brønsted acid sites of sample NH-7, however the sample exhibits low selectivity.

In summary, the semi-crystalline NH-7 sample grafted with propylamine groups, is the best alternative if we consider the yield of the acrylate product. Nevertheless, if we consider formation of a pure product, the amorphous NH-0 is the most promising. This sample has a similar acrylate yield but 91% selectivity. The yield can be enhanced by increasing the reaction time, thus sample NH-0 can show a higher yield while maintaining very high selectivity.

Conclusions

Amorphous and semi-crystalline samples with MFI type framework structure were synthesized by varying the hydrothermal synthesis time. As crystallinity of the samples increased, the number and strength of Brønsted acid sites increased too. Interestingly, even with a small amount of BAS, the H-7 sample has the same strength as the fully cryatlline samples (???). Due to the more open structure, the higher turnover frequency in the acidic deacetalization step of sample ???? was measured. The APTMS was grafted on the samples to introduce basic sites. The silanol type was revealed to be a crucial factor affecting the grafting capacity of the samples. With higher concentration of external silanols, the amorphous sample (H-0) presented the best anchoring capacity and, therefore, the higher selectivity to the acrylate product in the Knoevenagel condensation step.

Acknowledgments

This work was supported by FAPESP (Fundação de Amparo à Pesquisa do Estado de São Paulo) [grant number 2016/21033-2] and CAPES (Coordenação de Aperfeiçoamento de Pessoal de Nível Superior – Brasil) [grant number 001].

References

[1] M.J. Climent, A. Corma, S. Iborra, M.J. Sabater, Heterogeneous catalysis for tandem reactions, ACS Catal. 4 (2014) 870–891. https://doi.org/10.1021/cs401052k.

[2] J.M. Fraile, R. Mallada, J.A. Mayoral, M. Menøndez, Shift of Multiple Incompatible Equilibriums by a Combination of, (2010) 3296–3299. https://doi.org/10.1002/chem.200902759.

[3] M.H. Qi, M.L. Gao, L. Liu, Z.B. Han, Robust Bifunctional Core-Shell MOF@POP Catalyst for One-Pot Tandem Reaction, Inorg. Chem. 57 (2018) 14467–14470. https://doi.org/10.1021/acs.inorgchem.8b02303.

[4] R. Javad Kalbasi, A. Khojastegi, Hierarchically Pore Structure poly 2-(Dimethyl amino) ethyl methacrylate/Hi-ZSM-5: A Novel Acid–Base Bi-functional Catalyst as Heterogeneous Platform for a Tandem Reaction, Catal. Letters. 148 (2018) 958–971. https://doi.org/10.1007/s10562-018-2301-z.

[5] T. Ge, Z. Hua, Y. Zhu, Y. Song, G. Tao, X. Zhou, L. Chen, W. Ren, H. Yao, J. Shi, Amine-modified hierarchically structured zeolites as acid-base bi-functional catalysts for one-pot deacetalization-Knoevenagel cascade reaction, RSC Adv. 4 (2014) 64871–64876. https://doi.org/10.1039/c4ra11865k.

[6] P. Peng, D. Stosic, X. Liu, Z. Yan, S. Mintova, Strategy towards enhanced performance of zeolite catalysts : Raising e ff ective di ff usion coe ffi cient versus reducing

di ff usion length, 385 (2020). https://doi.org/10.1016/j.cej.2019.123800.

[7] X. Jia, W. Khan, Z. Wu, J. Choi, A.C.K. Yip, Modern synthesis strategies for hierarchical zeolites: Bottom-up versus top-down strategies, Adv. Powder Technol. 30 (2019) 467–484. https://doi.org/10.1016/j.apt.2018.12.014.

[8] T. Ge, Z. Hua, Y. Zhu, Y. Song, G. Tao, X. Zhou, L. Chen, W. Ren, H. Yao, J. Shi, Amine-modified hierarchically structured zeolites as acid-base bi-functional catalysts for one-pot deacetalization-Knoevenagel cascade reaction, RSC Adv. 4 (2014) 64871–64876. https://doi.org/10.1039/c4ra11865k.

[9] A. Talebian-Kiakalaieh, S. Tarighi, Hierarchical faujasite zeolite-supported heteropoly acid catalyst for acetalization of crude-glycerol to fuel additives, J. Ind. Eng. Chem. 79 (2019) 452–464. https://doi.org/10.1016/j.jiec.2019.07.021.

[10] J.G.P. Vicente, P.M. Lima, D. Cardoso, Nanosized Particles of X Zeolite Containing Ammonium Cations as Basic Catalysts, Catal. Letters. 147 (2017) 880–892. https://doi.org/10.1007/s10562-017-1969-9.

[11] I.L. Motta, J.G.P. Vicente, D. Cardoso, Properties and catalytic evaluation of nanometric X zeolites containing linear alkylammonium cations, Mol. Catal. 458 (2018) 127–138. https://doi.org/10.1016/j.mcat.2018.02.025.

[12] S. Inagaki, K. Thomas, V. Ruaux, G. Clet, T. Wakihara, S. Shinoda, S. Okamura, Y. Kubota, V. Valtchev, Crystal growth kinetics as a tool for controlling the catalytic performance of a FAU-type basic catalyst, ACS Catal. 4 (2014) 2333–2341. https://doi.org/10.1021/cs500153e.

[13] K.G. Haw, J.P. Gilson, N. Nesterenko, M. Akouche, H. El Siblani, J.M. Goupil, B. Rigaud, D. Minoux, J.P. Dath, V. Valtchev, Supported Embryonic Zeolites and their Use to Process Bulky Molecules, ACS Catal. 8 (2018) 8199–9212. https://doi.org/10.1021/acscatal.8b01936.

[14] L.L. Silva, D. Cardoso, C. Sievers, L. Martins, Evolution of Structure and Active

Sites during the Synthesis of ZSM-5: From Amorphous to Fully Grown Structure, J. Phys. Chem. C. 124 (2020) 2439–2449. https://doi.org/10.1021/acs.jpcc.9b09438.

[15] I.W. Zapelini, D. Cardoso, (Proof), Microporous Mesoporous Mater. (2021). https://doi.org/10.1016/j.micromeso.2021.111270.

[16] K.G. Haw, J.M. Goupil, J.P. Gilson, N. Nesterenko, D. Minoux, J.P. Dath, V. Valtchev, Embryonic ZSM-5 zeolites: Zeolitic materials with superior catalytic activity in 1,3,5-triisopropylbenzene dealkylation, New J. Chem. 40 (2016) 4307–4313. https://doi.org/10.1039/c5nj03310a.

[17] C.D. Chang, A.T. Bell, Studies on the mechanism of ZSM-5 formation, Catal. Letters. 8 (1991) 305–316. https://doi.org/10.1007/BF00764192.

[18] I.W. Zapelini, D. Cardoso, Amine-grafted Na-LTA zeolite precursors as basic catalysts for Knoevenagel condensation, Microporous Mesoporous Mater. (2021). https://doi.org/10.1016/j.micromeso.2021.111270.

[19] S.D. Kim, S.H. Noh, K.H. Seong, W.J. Kim, Compositional and kinetic study on the rapid crystallization of ZSM-5 in the absence of organic template under stirring, Microporous Mesoporous Mater. 72 (2004) 185–192. https://doi.org/10.1016/j.micromeso.2004.04.024.

[20] J.H. de Boer, B.C. Lippens, B.G. Linsen, J.C.P. Broekhoff, A. van den Heuvel, T.J. Osinga, Thet-curve of multimolecular N2-adsorption, J. Colloid Interface Sci. 21 (1966) 405–414. https://doi.org/10.1016/0095-8522(66)90006-7.

[21] J. Datka, A.M. Turek, J.M. Jehng, I.E. Wachs, Acidic properties of supported niobium oxide catalysts: An infrared spectroscopy investigation, J. Catal. (1992). https://doi.org/10.1016/0021-9517(92)90279-Q.

[22] M. Thommes, K. Kaneko, A. V. Neimark, J.P. Olivier, F. Rodriguez-Reinoso, J. Rouquerol, K.S.W. Sing, Physisorption of gases, with special reference to the evaluation of surface area and pore size distribution (IUPAC Technical Report), Pure Appl. Chem. 87

(2015) 1051–1069. https://doi.org/10.1515/pac-2014-1117.

[23] C. Morterra, G. Magnacca, A case study: Surface chemistry and surface structure of catalytic aluminas, as studied by vibrational spectroscopy of adsorbed species, Catal. Today. (1996). https://doi.org/10.1016/0920-5861(95)00163-8.

[24] T.K. Phung, L. Proietti Hernández, A. Lagazzo, G. Busca, Dehydration of ethanol over zeolites, silica alumina and alumina: Lewis acidity, Brønsted acidity and confinement effects, Appl. Catal. A Gen. (2015). https://doi.org/10.1016/j.apcata.2014.12.047.

[25] R.W. Thompson, Comments on the autocatalytic nucleation of (Na, TPA)-ZSM-5, Zeolites. (1992). https://doi.org/10.1016/0144-2449(92)90058-W.

[26] E. Lippmaa, A. Samoson, M. Mägi, High-Resolution 27A1 NMR of Aluminosilicates, J. Am. Chem. Soc. (1986). https://doi.org/10.1021/ja00268a002.

[27] L. Treps, C. Demaret, D. Wisser, B. Harbuzaru, A. Méthivier, E. Guillon, D.V. Benedis, A. Gomez, T. De Bruin, M. Rivallan, L. Catita, A. Lesage, C. Chizallet, Spectroscopic Expression of the External Surface Sites of H-ZSM-5, J. Phys. Chem. C. (2021). https://doi.org/10.1021/acs.jpcc.0c10200.

[28] E. Dib, I.M. Costa, G.N. Vayssilov, H.A. Aleksandrov, S. Mintova, Complex H-bonded silanol network in zeolites revealed by IR and NMR spectroscopy combined with DFT calculations, J. Mater. Chem. A. (2021). https://doi.org/10.1039/d1ta06908j.

[29] K. Barbera, F. Bonino, S. Bordiga, T.V.W. Janssens, P. Beato, Structure-deactivation relationship for ZSM-5 catalysts governed by framework defects, J. Catal. (2011). https://doi.org/10.1016/j.jcat.2011.03.016.

[30] I.C. Medeiros-Costa, E. Dib, F. Dubray, S. Moldovan, J.P. Gilson, J.P. Dath, N. Nesterenko, H.A. Aleksandrov, G.N. Vayssilov, S. Mintova, Unraveling the Effect of Silanol Defects on the Insertion of Single-Site Mo in the MFI Zeolite Framework, Inorg. Chem. 61 (2022) 1418–1425. https://doi.org/10.1021/acs.inorgchem.1c03076.

[31] E.S. Sanz-Pérez, A. Fernández, A. Arencibia, G. Calleja, R. Sanz, Hybrid amine-

silica materials: Determination of N content by 29Si NMR and application to direct CO2 capture from air, Chem. Eng. J. 373 (2019) 1286–1294. https://doi.org/10.1016/j.cej.2019.05.117.

Supporting information

Amine-grafted H-MFI zeolite precursors as acidic-basic catalysts for deacetalization-Knoevenagel condensation

Iago William Zapelini [a,b], Laura Lorena da Silva [c], Svetlana Mintova [b], Dilson Cardoso [a]

[a] Laboratório de Catálise, Universidade Federal de São Carlos - São Carlos 13565-905, Brasil.

[b] Laboratoire Catalyse et Spectrochimie, ENSICAEN, Université de Caen - Caen 14050, France.

[c] Grupo de Pesquisa em Catálise, Instituto de Química, Universidade Estadual Paulista - Araraquara 14800-900, Brasil.

Figure S1. XRD pattern of H-7 sample. Asterisks indicate the initial crystallization of MFI phase.

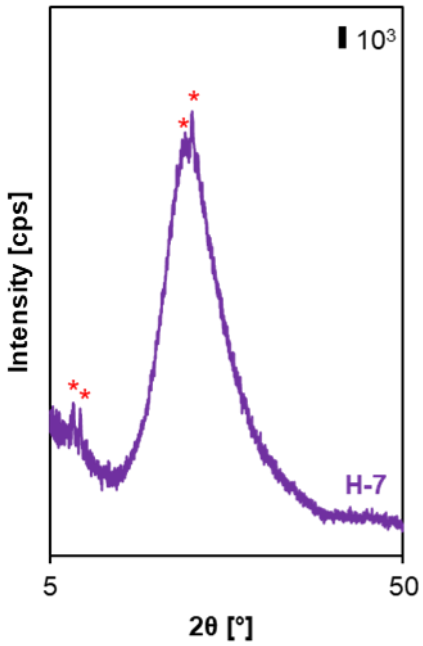

Figure S2. XRD patterns of NH-*x* samples.

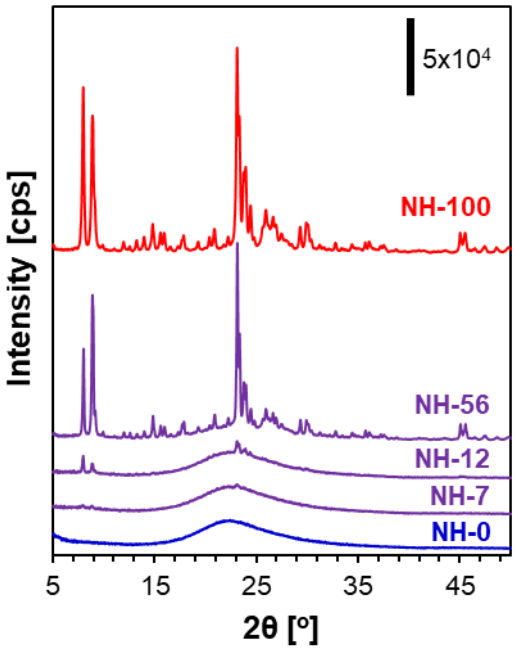

Figure S3. t-plot curves of H-*x* samples.

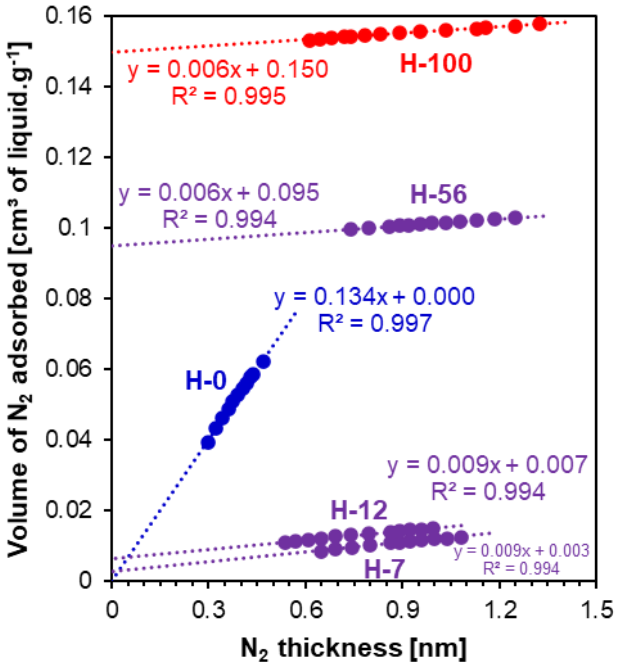

Figure S4. TEM images of H-0 and H-12 samples (scale bar = 100 nm).

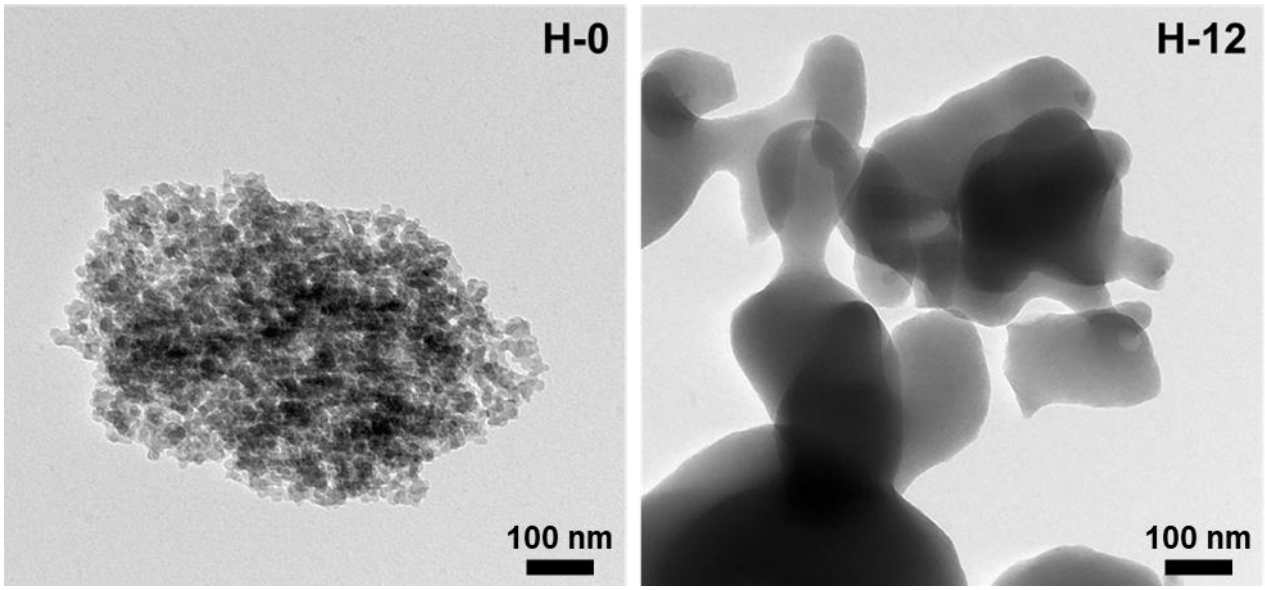

Figure S5. ^{13}C MAS NMR spectrum of sample NH-0.

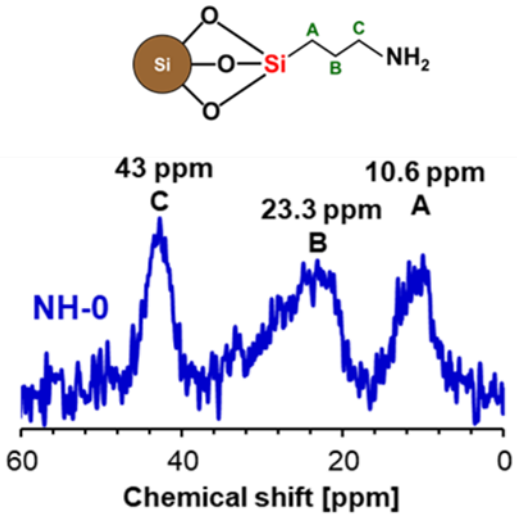

Figure S6. Correlation between nitrogen loading in NH-x samples and the selectivities to acrylate end product in 4 h catalytic test.